Title

More than expected: extracellular waveforms and functional responses in monkey LGN

Authors

Shi Hai Sun[1,2], Nathaniel J. Killian[3], John S. Pezaris[1,2]

Affiliations

[1]Department of Neurosurgery, Massachusetts General Hospital, Boston, MA, USA

[2]Department of Neurosurgery, Harvard Medical School, Boston, MA, USA

[3]Department of Neurological Surgery, Albert Einstein College of Medicine, Bronx, NY, USA

Conflicts of interest

No conflicts of interest.

Abstract

Unlike the exhaustive determination of the retina, key populations in the lateral geniculate nucleus of the thalamus (LGN) may have been missed. Here, we have begun to characterize the full range of extracellular neuronal responses in the LGN of awake monkeys using multi-electrodes during the presentation of colored noise visual stimuli to identify any previously overlooked signals. The extracellular spike waveforms of single units were classified into seven distinct classes: four negative-dominant classes that were narrow or broad, commonly associated with inhibitory or excitatory neurons, respectively; one triphasic class; and two positive-dominant classes. These units had their receptive fields (RF) mapped using spike-triggered averaging and were classified into magnocellular (*M*), parvocellular (*P*), koniocellular (*K*), and non-RF (*N*) neurons. Spike classes were correlated with their mapped RF and response characteristics to identify any relationships between spike shape and cell type: negative and narrow spiking waveform units had RFs that were mostly *P*; negative and broad waveform units, mostly *N*; and positive waveform units, mostly *M*, as well as having shorter response latencies, larger RF sizes, and larger eccentricities than the other waveform classes. *N* cells, those without an estimated RF, have not been regularly reported before. We observed that most *N* cells consistently responded to the visually presented noise stimulus at a lower and more sustained rate than units with an RF. Our observations indicate that the population of LGN cells may be broader than traditionally held.

Significance Statement

This study aims to extensively survey the extracellular space in the LGN of rhesus macaques. We found significant functional differences across extracellular waveform classes, such as their receptive field (RF) and spiking characteristics (e.g., firing rate, burstiness, latency). We also found a set of single units that did not yield an RF but reliably responded to the visually presented stimuli. Our findings reveal that the neural population of LGN may extend beyond the classical divisions of magnocellular, parvocellular, and koniocellular responses. This new finding will have interesting implications for our understanding of LGN function and interpretation of extracellular signals, especially significant with the recent advancement of dense multi-electrode arrays.

Introduction

A critical early structure for carrying and processing visual information in mammals is the lateral geniculate nucleus (LGN) of the thalamus, the primary relay center between the retina and the visual cortex (Sherman & Guillery, 2006; Solomon & Lennie, 2007). In primates, the LGN is anatomically separated into layers of magnocellular (M), parvocellular (P), and koniocellular (K). Primate electrophysiological studies have shown that M, P, and K neurons differ in their stimulus and response dynamics: M neurons have fast temporal dynamics, well suited for motion detection; P neurons are sensitive to chromatic dynamics, well suited for color and form processing; and K neurons receive input from short-wavelength ("blue") photoreceptors (Wiesel & Hubel, 1966; Schiller & Malpeli, 1978; Kaplan & Shapley, 1982; Derrington & Lennie, 1984; Hubel & Livingstone, 1990; Maunsell *et al.*, 1999; Reid & Shapley, 2002; Tailby *et al.*, 2008).

Although these divisions have been extensively characterized (K neurons to a lesser extent), much of our knowledge about the function of the LGN has been obtained from electrophysiological recordings using single-channel electrodes to identify neuronal response in the form of extracellular spikes. The waveform of these signals is typically biphasic with a dominantly negative voltage excursion and can, to an extent, be used to determine a neuron's cell type: excitatory if the waveform is broader and inhibitory if the waveform is narrower (Henze *et al.*, 2000). With the recent advancement of dense multi-electrode arrays and sophisticated spike-sorting algorithms, there has been a substantial increase in the variation of spike waveform shapes reported in multiple species and brain regions that are poorly understood. These waveform variations include triphasic-spiking waveforms found in rat hippocampus (Barry, 2015) and superior colliculus (Sibille *et al.*, 2022); positive-spiking and long-broad negative waveforms found in the cat visual cortex (Gold *et al.*, 2009; Sun *et al.*, 2021) and human prefrontal cortex (Paulk *et al.*, 2022); and doublet-spiking waveforms consisting of two short downward deflections found in ferret LGN (Murphy *et al.*, 2020). All the waveforms described above differed from the classic biphasic and negative waveforms, which may have been overlooked in earlier studies due to the sampling biases inherent in traditional single electrodes (Olshausen & Field, 2005; Talebi & Baker, 2016). Accordingly, key populations may have been missed; identifying the gamut of extracellular signals from the LGN may help in understanding the processing in the visual pathway.

Thus, in this study, we agnostically survey the extracellular space in the LGN of rhesus macaques through recordings that were not optimized for single unit isolation, employing a variety of stimulus and electrode properties. For every LGN unit recorded, we recovered its receptive field (RF) class and extracellular spike waveform class, along with several response metrics to identify relationships between spike shape and possible neuronal type. We also recovered a set of units without an estimated RF (non-RF, N units) that are not

regularly reported, with most of these units consistently responsive to the visually presented stimulus at a lower and more sustained response rate than units with an RF. The presence of N cells hints that the LGN may require understanding beyond the classification into M, P, and K responses, and insight into these nuances could reveal computations in the visual system that have yet to be discovered.

Methods

Ethics

Recordings were made from three awake adult rhesus monkeys (*Macaca mulatta*, 3M, 19–20 kg). The animals were maintained in the animal facility at the Massachusetts General Hospital. All research procedures were approved by the Massachusetts General Hospital Institutional Animal Care and Use Committee (IACUC) and were carried out according to the NIH Guide for the Care and Use of Laboratory Animals.

Animal preparation

The animals were surgically implanted with titanium head-holding posts and recording cylinders that allowed bilateral access to the LGN. Animals were trained to sit in a primate chair (B & M Plastics, Inc.), and placed in a shielded recording chamber (Crist Instrument Co.) during recordings. The animals were positioned so that their eyes were 43 cm from a 22-inch CRT monitor (Viewsonic P220f) with neutral gaze position near the center of the monitor.

Gaze location was monitored by an infrared video camera at a 500 Hz sampling rate (SensoMotoric Instruments GmbH, High-Speed Primate), with infrared illuminators stacked to yield a single corneal reflection. Software (iView X, SensoMotoric Instruments) was used to adjust the gains and offsets of the pupil-corneal reflection distance. Gaze position signals were then sent via analog signals to a behavioral control computer, where additional calibration was performed (2D quadratic fit to nine calibration points). See Figure 1A for a schematized depiction of the recording cylinder, monitor positioning and eye tracking.

Behavioral task

A trial-based task was used to map the response fields of neurons (Figure 1B). To begin each trial, the animal was required to fixate on a centrally presented small, circular target (0.2° diameter white spot) for 400 ms. The visual mapping stimulus then began with the fixation point continuing to be visible overlaid on the animated noise, and the animal was required to continue maintaining fixation within a 2.0° diameter circular window for the duration of the stimulus (2.5–5.0 seconds, mode of 2.5 seconds; typical fixation performance was much tighter than this window; see Results). Successful fixations through the entire stimulus were rewarded with drops of sweet liquid and pleasant audio feedback. Data from successful trials were used for mapping analysis (4–215 trials per experiment, median of 32 trials), but data from all trials were used for the spike waveform analysis.

Visual Stimuli

Custom software (PLECS, Pezaris Lab Experiment Control System) was used to display noise stimuli that spanned both luminance and chrominance spaces, in addition to controlling behavioral state and data collection (Killian *et al.*, 2016). The visual stimuli were presented on a CRT display (Viewsonic P220f) at 160 Hz refresh rate and 8 bits per color channel on a display area of 40 by 30 cm (400 by 300 pixels) that subtended 53° by 40° in visual field. Two classes of noise stimuli were presented: high-resolution 400 by 300 pixel sets with power spectra proportional to one over frequency (five sets, described below) and low-resolution 80 by 60 pixels with a white power spectrum (one set). Each recording used a single mapping stimulus from this collection.

The high-resolution noise stimuli were generated through computations in the frequency domain:

$$\xi = \left(\xi_x, \xi_y, \xi_t\right) \tag{1}$$

$$S(\xi) = \frac{1}{\|\xi\|^{\beta}} \tag{2}$$

$$|(Ff)(\xi)|^2 = S(\xi) \tag{3}$$

$$Ff(\xi) = \left(S(\xi)\right)^{1/2} e^{-i2\pi\varphi} \tag{4}$$

$$\varphi = rand[0,1] \tag{5}$$

$$f(x, y, t) = F^{-1}(Ff)(x, y, t) \tag{6}$$

where ξ is the spatiotemporal frequency vector represented in space (x, y) and time (t), $S(\cdot)$ is the power spectra, β is a set variable of 0, 1.5, 2.5, 3.14, 3.5, or 4.0; F is the Fourier transform; and $f(x, y, t)$ in the value of each pixel in space and time. Increasing values of β decrease the slope of the power spectrum, where a β value of 0 yields a white spectrum (used here for 80 by 60-pixel stimuli), and higher values of β yield more naturalistic spectra with higher spatial and temporal correlations (Simoncelli & Olshausen, 2001). See Extended Figure 1-1 for illustrated examples.

Electrode implantation

LGN recordings were made with acutely inserted electrodes (n = 98 recordings; 75 multichannel recordings, 22 single-channel recordings; three animals) or chronically implanted electrodes (n = 12 recordings; one animal). Acute electrodes were either a custom single linear 16-electrode array with 200 µm or 260 µm channel spacing, a linear 16-electrode tetrode configuration array (four groups of four contacts) with 50 µm intra-group

spacing and 450 µm inter-group spacing (Plexon U-Probe), or a single traditional tungsten electrode (FHC, Inc.). Chronic electrodes were custom 64-channel microwire bundles designed to splay at depth.

Before acute penetration, the recording chamber was opened and cleaned, the micromanipulator attached (Model 650, Kopf Instruments), and used to advance the electrode to the area of interest. Neural responses were recorded by a data acquisition system (Power 1401, Cambridge Electronic Design) and software (Spike 2, Cambridge Electronic Design) that sampled at 40 kHz for all electrodes and channels, to 16-bit resolution. Unless stated otherwise, the data presented in this project are from electrodes with multiple channels (single-channel electrode data from traditional tungsten electrodes are shown only in Figures 4D and 5C).

Spike sorting

Extracellular recordings can have spikes from multiple nearby neurons recorded on the same channel, and for multi-electrode channels, spikes from the same neuron may appear on multiple channels. To distinguish spikes from different neurons, extracellular signals were automatically sorted through KiloSort 2.5 (Pachitariu *et al.*, 2016). The output was then manually curated with *phy* (Rossant *et al.*, 2016). During manual curation, clusters were cleaned by drawing a boundary in the principal component analysis (PCA) space to remove any abnormal waveforms. The clusters were then assigned a label of *good* or *noise. Good* clusters showed evidence of a refractory period (longer than 1 ms) in the autocorrelogram with a dip to approximately zero, and clear isolation from other clusters in PCA space. Merges were made between *good* clusters if they had similar waveforms (overlapping PCAs), a shared refractory period (central dip in their crosscorrelogram), or if there was evidence of

drift (one cluster halts spiking when the other starts at an adjacent channel). The lack of an autocorrelogram-like shape in the crosscorrelogram would disqualify a merge. All *good* clusters were identified as single units (SU). The remaining *noise* clusters were not included in additional analysis.

Extracellular spike waveform analysis

We will represent a single unit's extracellular signal by its mean extracellular spike waveform, which is then analyzed and compared to the mean waveform of other single units. To obtain the mean waveform of each single unit, *u*, up to 2,000 spike waveforms, *k*, were extracted from the raw signal, randomly selected from identified firing times for that neuron and collected as a set W_u^k (Figure 1C). Each waveform was extracted from a window of 60 samples (1.5 ms) before to 120 samples (3 ms) after the selected spike time; extracted single waveforms were then averaged together to obtain the mean waveform $\overline{W_u}$. If a single unit produced less than 2,000 spikes, then all spikes were used (this limitation occurred with 44% of units). For multi-channel electrode recordings, all channels were sampled and averaged, with the single channel with the largest mean spike waveform amplitude selected as the mean waveform for each of those cells. Through the remainder of this report, we will use *spike waveform* to refer to the mean extracellular waveform of a single unit, $\overline{W_u}$ from the channel with the largest signature.

Spike waveform classification

Mean waveforms, $\overline{W_u}$, were automatically classified using WaveMAP (Lee *et al.*, 2021), which uses Uniform Manifold Approximation and Projection (UMAP; McInnes *et al.*, 2020) for dimensionality reduction and the Louvain method for cluster identification (Blondel *et al.*, 2008). As in Lee *et al.* (2021), before WaveMAP classification, the mean waveform of each single unit, $\overline{W_u}$, was normalized so that the maximum of its absolute value was 1.

Receptive Field Analysis

Spike-triggered averaging

Each single unit's chromospatiotemporal (CSTRF, or just RF) was estimated by computing a spike-triggered average (STA; Schwartz *et al.*, 2006), which averages the visual stimulus around each spike time by the following formula:

$$STA = \frac{1}{N}\sum_{i} s_i \qquad \textit{Eq. 1}$$

where s_i represents the stimulus in a fixed-size temporal window spanning the time of the ith spike, and N is the total number of spikes. The STA was computed using 25 stimulus frames before to 10 frames after each spike (i.e., time lags of –25 to 10 frames, or –156.25 ms to 62.5 ms in steps of 6.25 ms). The entire STA was then whitened by multiplying it with the stimulus covariance matrix (Sharpee, 2013). The resulting chromospatiotemporal receptive field is in four dimensions: time, position in the horizontal dimension, position in the vertical dimension, and color by phosphor (red, R; green, G; blue, B).

RF position and latency

The position of each RF was determined by the location of the maximum excursion across the RF. The process of identifying RF position was performed iteratively: a first pass was used to find the absolute maximum; a second pass, to determine the background noise after clipping out a rectangular region 4 degrees on a side centered spatially at the maximum and spanning all time; and a third pass, to enforce statistical selection constraints based on *z*-score. The localization of the peak value was performed in luminance space after converting the CSTRF by taking the vector length of the RGB components for each pixel:

$$Lum_{x,y,t} = \sqrt{{R_{x,y,t}}^2 + {G_{x,y,t}}^2 + {B_{x,y,t}}^2} \qquad \textit{Eq. 2}$$

$$RF_{location} = argmaxLum_{x,y,t} \qquad \textit{Eq. 3}$$

where R, G, and B are the intensity of the colored phosphors red, green, and blue, respectively, and x, y, and t are locations in the CSTRF matrix in *x*-space, *y*-space, and time, respectively. The luminance matrix, Lum, was determined by the magnitude of the colored phosphors. From Lum, the 3-tuple representing the position of its maximum was recorded as the spatiotemporal location of the RF. Throughout this report, *RF position* refers to the *x* and *y* spatial components of $RF_{location}$, *RF latency* refers to its temporal component, and RF_{max} to the spatial plane at the latency point. Lum_{max} is the luminance value of RF_{max}.

RF size and RF spatial window

The RF size and spatial window were measured from the spatial envelope of Lum_{max}. First, a 2D Gaussian fit was applied to Lum_{max}, and then the length and width of the RF were defined as the full width at 60% maximum (i.e., one standard deviation) along the vertical

and horizontal directions, respectively, and corrected for cosine error. The RF size was defined as the average of length and width, and the RF spatial window as the area length times width. All data referring to RF size in this study are from receptive fields from which a clean spatial envelope could be extracted when mapped using high-resolution stimuli (n = 128).

RF temporal window

A temporal window was used to select frames around the peak by fitting a two-term Gaussian model to $Lum_{x,y}$ at the RF position, through time. If the polarity of RF_{max} was *off*, pixels were multiplied by -1 before fitting. Frames where this value at least one standard deviation above the noise level and were of the same polarity as RF_{max} were considered the RF temporal window.

***Z*-score**

To evaluate the strength of each RF and impose statistical constraints, we computed its *z*-score, its amplitude a divided by the noise level η. The amplitude was computed as an un-normalized peak value by averaging the CSTRF pixels within the spatial and temporal windows. This average value, an RGB triplet, was then transformed to luminance space to obtain the RF amplitude a. The noise floor η was determined by the standard deviation of amplitude computed in the same manner with an equivalent number of pixels, but taken randomly from RF_{noise}, the acausal frames (frames after the spike, thus positive latencies) of the CSTRF, and repeated without replacement until all pixels in RF_{noise} were used. Normalizing the amplitude by the noise floor yielded the *z*-score for the RF: $z = a / \eta$.

Cone Weights Calculation

We used the method described in Horwitz & Albright (2005) to obtain the RF color weights (RGB; red, green, and blue phosphor intensities, also known as *gun values*) and then converted those values to cone weights (LMS; corresponding to sensitivities for long, medium, and short wavelength cones). The color weights were obtained by computing the mean STRF value within the spatial and temporal windows and then converting to cone weights by the following formula:

$$[\mathrm{LMS}] = A^{-T} * [RGB]^{T} \qquad \textit{Eq. 4}$$

where A^{-T} is the inverse transpose of the three-by-three transformation matrix, A. To obtain the transformation matrix, *RGB* gun values from the CRT were computed for each color channel in independent trials. Spectral radiance values were measured (PR650 SpectraScan Colorimeter, Photo Research, Inc), and the transformation matrix was obtained from pairwise inner products of the monitor spectral radiance values and 10° cone fundamentals (Stockman & Sharpe, 2000). The LMS cone weights were then normalized by dividing each cone weight by the sum of their absolute weights.

Cone weight noise

For each of the three cone weights in an RF, a corresponding noise level was measured to determine significance. The noise levels were calculated analogously from the acausal pixels presumed not to contain signal as described for η above, except, instead of transforming the averaged pixels into luminance space, those pixels were transformed into cone space using

Equation 4. The noise threshold for each cone weight was then taken as one standard deviation of the corresponding cone space values derived from acausal pixels.

Response metrics

PSTH responsiveness and response latency

The peristimulus time histogram (PSTH) was used to determine responsiveness and response latency for each cell. The PSTH was computed during the time range 600 ms before stimulus onset through the end of stimulus presentation, binned to 1 ms. Responsiveness was determined by comparing bins that were 600–0 ms before to those 200–800 ms after stimulus onset (paired Student's t-test, $p < 0.05$). When estimating the stimulus response latency, the PSTH was smoothed by applying a running average over a sliding window of length 5 ms, and the response latency was determined by the delay between stimulus onset and when the firing rate crossed 50% between baseline and maximum value during stimulus presentation.

Burst index

To describe the firing patterns of LGN cells, we used a burst index which measured how bursty (bunched together in time) or tonic (evenly spread out) a spike train is. Bursts were defined by an inter-spike interval of greater than 100 ms, followed by a string of inter-spike intervals of less than 4 ms. The burst index was then computed as the ratio of spikes occurring in a burst over all spikes in the spike train (Sherman, 2001; Wang *et al.*, 2006).

Single Unit Screening

To remain agnostic about cellular responses while maintaining confidence that recorded cells were from within LGN, we used a screening criterion that started with each well-isolated cell for which an RF was found (n = 214; RF units) and then included all other well-isolated cells appeared on the same channel (n = 67; non-RF units). This screening method resulted in 281 units from 87 experiments spanning three animals.

Statistical Analysis

Several statistical analyses and significance comparisons are made throughout this study. All results are shown as the mean with standard deviation (SD), except for Figure 4B, which uses mean with standard error of the mean (SEM). Significance tests involving the mean were done with unpaired Student's *t*-tests unless stated otherwise. All statistical analyses were performed using MATLAB.

Results

Extracellular spike waveforms

The spike waveforms of 281 single units (SUs) were recorded from 87 electrode penetrations in the LGN of three macaques (M_{CH}, n = 104; M_{ST}, n = 51; M_{VG}, n = 126) and were classified using WaveMAP (Lee *et al.*, 2021), producing seven distinct spike waveform classifications. Four were the commonly reported negative-spiking waveform (Figure 2 left side): a dominant

negative deflection followed by a smaller and slower positive deflection. The differences between these four groups are their width (i.e., trough-to-peak duration) and the magnitude of positive deflection (trough-to-peak ratio). Negative-spiking waveforms are often classified into broad- and narrow-spiking classes, which have been associated with excitatory and inhibitory neurons, respectively (Barthó *et al.*, 2004). Therefore, we defined these four classes as *Narrow 1* (N1, *n* = 34, 12%, shown as dark blue in Figures 2 and 5), *Narrow 2* (N2, *n* = 60, 21%, purple), *Broad 1* (B1, *n* = 47, 17%, orange), and *Broad 2* (B2, *n* = 14, 5%, light blue).

The insets under the grouped waveforms within Figure 2 (visualized as smaller waveforms) show some of the variability within each waveform class. For example, within the four negative-spiking classes, a small population were doublet-spiking waveforms (6%, *n* = 11/191; see right insets of N2 and B2 in Figure 2), where the spike waveform consisted of two distinct negative deflections (examined qualitatively). These doublet-waveforms consisted of N2 (73%, *n* = 8/11), B1 (9%, *n* = 1/11), and B2 units (18%, *n* = 2/11), and none were N1 units. See Discussion for possible justifications of doublet waveforms along with all other spike waveforms mentioned in this study.

The fifth spike waveform class was also negative spiking but had the addition of an initial positive deflection preceding the primary, negative deflection, and subsequent positive deflection, which creates a distinct *Triphasic* shape (T, *n* = 36, 13%, green). Even though we defined this group as triphasic, not all units had three distinct phases when examined qualitatively (81% qualitatively triphasic, *n* = 29/36; see Figure 2 insets for examples).

The remaining two classes were positive spiking, which we defined as *Positive 1* (P1, n = 50, 18%, black) and *Positive 2* (P2, *n* = 40, 14%, red). We noticed two main differences between these two positive classes. Firstly, P1 waveforms featured a larger negative deflection than those from P2; secondly, P2 as a class had a higher proportion of waveforms

with two prominent positive peaks surrounding a negative deflection (i.e., M-shaped; see examples in Figure 2 under the grouped waveforms). The P1 and P2 classes had 6% (*n* = 3/50) and 55% (*n* = 22/40) M-shaped positive spikes, respectively, when qualitatively examined. Positive and triphasic-shaped extracellular waveforms have not been commonly reported in previous studies but have recently been linked to recordings of action potentials propagating through axonal fibers (Meeks *et al.*, 2005; Gold *et al.*, 2006; Lewandowska *et al.*, 2015), and afferent fibers originating from preceding processing areas (Barry, 2015; Sun *et al.*, 2021; Sibille *et al.*, 2022), i.e., from the retina in our case here.

Receptive fields: RF and non-RF units

All 281 SUs were presented with chromatic noise visual stimuli (see Methods) to estimate their chromospatiotemporal receptive field (CSTRF, or just RF) by computing the spike-triggered average (STA, see Methods). SUs with successful CSTRF mapping had a *z*-score of greater than three (see Extended Figure 3-1A for *z*-score distribution), which we will term as *RF units* (*n* = 214/281, 76%), and nearly all CSTRFs had a lower spatial variance than the gaze location (*n* = 116/128, 91%; Extended Figure 3-1B). The remaining SUs without successful CSTRF mapping are termed *non-RF units* or *N units* (*n* = 67/281, 24%). In this study, we will examine both populations.

As mentioned in the Methods, two stimulus resolutions were used during RF mapping, coarse and fine (no cell was presented with both). The first two rows in Figure 3 illustrate two example RFs, one from a coarse stimulus (RF 1) and one from a fine stimulus (RF 2). Both examples have an *on*-center (responding to RGB increments) accompanied by an *off* rebound (responding to RGB decrements). These example cells demonstrate how fine stimuli allowed measurements of RFs with higher spatial resolution. However, we found that

this advantage came with the cost of a lower success rate at observing significant RFs than when using coarse stimuli (fine: 71%, n = 144/204; coarse: 91%, n = 70/77), likely due to the higher contrast in the coarse stimuli than the fine stimuli. This is evident in the striking surround estimated in RF 1 at –31.25 ms compared to the weak indication of a surround in RF 2. Since RF 1 was one of the few RFs that had a clear surround in our measurements, we will concentrate on RF centers.

M, P, and K classifications of RF units

The 214 mapped RFs were classified into magnocellular (M), parvocellular (P), or koniocellular (K) based on their relative responses to long-, middle- and short-wavelengths (LMS cone weights; Eq. 4). Firstly, RFs were classified into koniocellular if the S-cone weight had the largest magnitude (K, *n* = 15, 7%; see RF 5 in Figure 3 for an example); secondly, parvocellular if the L- and M-cone weights were opposing and significantly above noise (P, *n* = 66, 31%; RF 3 and 4 in Figure 3 for examples; see Discussion for justification of this definition of parvocellular response); and lastly, all remaining RFs classified as magnocellular (M, *n* = 133, 62%; RF 1 and 2 for examples), i.e., significant L- and M-cone weights that were of equal sign. It is important to note that this LGN cell classification is based on functional considerations, which are closely related to the anatomical classifications found in previous LGN studies (Wiesel & Hubel, 1966; Derrington *et al.*, 1984; White *et al.*, 1998; Reid & Shapley, 2002).

M, P, and K cone response characteristics

The relative contributions of the normalized *LMS* cone weights of all 214 RFs are visualized in the diamond plot of Figure 4A, as used in previous work comparing LGN neuron cone input (Derrington *et al.*, 1984; Reid & Shapley, 2002; Horwitz *et al.*, 2007). Aside from the dense cluster at the midpoint along the *LM*-on plane (top-right line of Fig. 4; e.g., RF 1), denoting even contribution from *L*- and *M*-cones, M RFs are distributed evenly across the whole *LM*-on and *LM*-off planes (bottom-left line) of the diamond. P RFs are clustered around the midpoint along the *L*-on and *M*-off plane (bottom-right line) but are more evenly spread along the *L*-off and *M*-on plane (top-left line). Lastly, nearly all of K RFs are *S*-cone *on* (n = 13/15, indicated by the high proportion of circular purple data points), and more than half (n = 8/15) are clustered in the bottom-left quadrant of Figure 4A, signifying an opposing contribution from *L*- and *M*-cones (i.e., *S*-on and *LM*-off). The 6:1 ratio of *S-on* to *S-off* RFs is consistent with previous studies in marmoset LGN (Martin & Lee, 2014; Pietersen *et al.*, 2014) and macaque retinal ganglion cells (De Monasterio *et al.*, 1975; De Monasterio & Gouras, 1975).

The *LMS* response over time for the RF center is called the *temporal weighting function* (TWF), tracing out the cone components inside the RF spatial window (see Methods) across frames (Reid & Shapley, 2002). There are noticeable differences in the TWFs between each of the RF classes. First, M and P RFs had opposing responses in *L*- and *M*-cone space, and second, in the number of phases: M units had two clear opposing phases in the TWFs to compute temporal changes while P units were monophasic to compute ordinary intensity. This biphasic versus monophasic profile of M and P RFs aligns with previous findings (Reid & Shapley, 2002). The chromatic opponency of P and non-opponency of M RFs align with their role in color vision, and both M and P units had little to

no S-cone response (9% and 7% relative to the peak cone response, respectively), which also aligns with previous work in macaque LGN (Callaway, 2005) and retinal ganglion cells (Sun *et al.*, 2006). Lastly, like P RFs, the TWF of K RFs were monophasic and chromatic opponent and with a moderate contribution from L- and M-cones (42% and 28% relative to peak, respectively).

M, P, and K spiking characteristics

Several response metrics that typically differentiate between M, P, and K neurons are also observed within our RF classes. First, within the area bound by the most eccentric K RF (5°, $n = 75$), the mean RF sizes of M (0.17° ± 0.06°) and P RFs (0.18° ± 0.07°) were significantly smaller than K RFs (0.32° ± 0.06°; $p = 10^{-8}$ and $p = 10^{-9}$, respectively). We also observed that although the rate of activity of M, P, and K units was not significantly different from each other ($p > 0.055$; M, 26.3 ± 20.1 spikes/s; P, 21.5 ± 13.83 spikes/s; K, 33.15 ± 19.8 spikes/s), the spiking activity of M units were more frequent in bursts (burst index of 0.064 ± 0.059) than the more tonic P (0.035 ± 0.044, $p < 10^{-2}$) and K units (0.017 ± 0.015, $p < 10^{-5}$). Not only did M units spend more time in bursts, but they also had shorter mean unsigned response latency (32.1 ± 7.9 ms) than P (42.60 ± 11.9 ms, $p < 10^{-9}$) and K units (–50.7 ± 7.9 ms, $p < 10^{-10}$), with P units having a significantly shorter response latency than K units ($p = 0.049$). Previous LGN studies have supported these differences between LGN RF types: RF size and response latency (Maunsell *et al.*, 1999; Pietersen *et al.*, 2014; Eiber *et al.*, 2018); but unsupported in our differences in burst spikes between RF classes (Ruiz *et al.*, 2006; Pietersen *et al.*, 2017).

We also found two unexpected differences between cells classified as M and P by RFs. Due to their larger cell bodies, we expected M units to have had the largest recorded

waveform amplitude out of the three classes. This was not the case with the M units in the current study ($p > 0.24$) (Figure 4C fifth row), likely because we did not optimize electrode position for each cell, and thus units were recorded at varying distances from the electrode tips (as amplitude is inversely proportional to source-to-site distance: Holt & Koch, 1999; Gold *et al.*, 2006). Second, we expected P units to be recorded more superficially than M units, given the anatomy of the LGN, but the mean estimated depths for M and K units were significantly more superficial than P units ($p < 0.009$) (Figure 4C sixth row). It is important to note that depth was estimated from the top of the recording chamber to the recording location, and does not provide a precise evaluation of recording depth from the cortical surface.

Non-receptive field (N) units

We then investigated N cells, the non-RF 24% ($n = 67/281$) of our population for which we were unable to develop a receptive field despite being recorded on the same channel as single units that did have measurable RFs. The significantly lower spiking activity of N units than RF units (N, 7.0 ± 9.6 spikes/s; RF, 22.3 ± 17.0 spikes/s; $p = 10^{-11}$; right side of Fig. 4D) would suggest that the visual stimulus did not activate these units, however more than half of N units had a significantly elevated firing rate during stimulus onset versus immediately before (59% of N units; paired t-test; see Methods; 83% for RF units). The lower spiking activity of N units may be evidence of insufficient data for a significant receptive field to be estimated, as RF quality as assessed by *z*-score was correlated with number of spikes in RF cells ($r = 0.63$). Not only did N units respond at a lower rate, but also at a more sustained rate than RF units (burst index of; N, 0.014 ± 0.013; RF, 0.035 ± 0.032; $p = 10^{-7}$). This variation in burstiness was moderately correlated with RF *z*-score (r = 0.46). We also report that N

units did not have a significantly different response latency than RF units (N, 43.9 ± 23.7 ms; RF, 46.6 ± 24.1 ms; $p = 0.67$; estimated from PSTHs: see Methods), implying that N units were unlikely to have been recordings of retinothalamic or corticothalamic projections from neighboring processing areas. There were also no significant differences in waveform amplitude ($p = 0.77$) and estimated depth ($p = 0.43$) between N and RF units, suggesting that the quality of the spike waveform and anatomical location were irrelevant to the recording of non-RF units.

We observed two experimental factors that did affect the N unit population. By including the single-channel units that were initially excluded from the dataset ($n = 48$), we found that there was a higher proportion of N units recorded with single-channel electrodes than multi-channel electrodes (44%, $n = 21/48$, versus 24%, $n = 67/281$; Figure 4E left panel). This discrepancy is perhaps due to the difference in electrode technology, as the single-channel electrodes used were sharper and had higher impedance than the multi-channel electrodes. Second, the proportion of N units recorded with coarse stimuli was much lower (9%, $n = 7/77$) than with fine stimuli experiments (24%, $n = 59/204$; Figure 4D right panel). The smaller fraction of N units from the coarse stimulus may be due to the stimulus' larger pixel size and higher contrast, driving neurons more strongly and perhaps driving a larger proportion of the population than the fine stimuli, as evident from its significantly higher spiking activity than units recorded with fine stimuli (coarse, 24.9 ± 20.3 spikes/s; fine, 16.3 ± 14.8 spikes/s; $p = 10^{-4}$).

Thus, in the N cells, we have observed a population of non-RF units that are not regularly reported. Compared to units for which we can extract an RF, we find that the majority of these units responded to the visual stimulus with lower and more sustained spiking activity but with no differences in waveform amplitude or recording depth compared

to units with RFs. The abundance of N units was also dependent on the electrode type and stimulus type used.

Correlations

With spike waveform classifications (N1, N2, B1, B2, T, P1, and P2), RF classifications (M, P, K, and N), and several response characteristics (e.g., spike-rate, response latency, RF size), in hand, we now turn to additional comparative analysis. When correlating spike waveform classifications to RF classifications (Figure 5A), we make three observations: (*i*) the two negative-spiking narrow classes (N1 and N2) had predominantly P RFs (35–53%) with approximately a 2-to-1 ratio to M RFs for N1 units and a 1-to-1 ratio for N2 units; (*ii*) the two negative-spiking broad classes (B1 and B2) had the largest proportion of N units (36–50%), compared to the lower proportion from all other waveform classes (15–28%); and (*iii*) the two positive-spiking classes (P1 and P2) were mostly M RFs (63–70%) with more than a 4-to-1 ratio to P RFs and the least proportion of K RFs (0–4%). This heterogeneity indicates there may be functional differences between waveform classes in the LGN but may also show evidence of a sampling bias (Towe & Harding, 1970). For example, the higher proportion of M RFs from the positive-spiking units may indicate the presence of more axonal projections from the deeper M layers (passing upward through the P layers as they flow toward the optic tract) than the P and K projections in our recordings.

A similar trend continues when comparing response characteristics (Figure 5B). Suppose we were to group the classical negative-spiking classes into narrow (N1 and N2) and broad (B1 and B2) and the non-traditional positive-spiking classes (P1 and P2) together. In that case, several distinct observations can be made. The positive classes responded to the visual stimuli with a significantly shorter response latency than all other classes ($p < 0.038$);

the RFs of narrow-negative classes were significantly smaller than all other classes ($p < 0.017$); and the RFs of positive and triphasic (T) classes were at a significantly larger eccentricity than the positive classes ($p < 0.020$). These observations are particularly significant because the shorter response latencies of the non-classical positive-spiking classes support the idea that these waveforms originate from axons in the retinothalamic projection, and, if the recorded positive waveforms are axonal, then it accounts for their higher eccentricities as eccentricity is positively correlated with axon diameter (Walsh *et al.*, 2000). Therefore, our observations show that the non-classical positive-spiking waveforms recorded in the LGN have distinct functional characteristics to the classical negative-spiking classes, similar to previous studies (cat V1: Sun *et al.*, 2021).

We also noted two additional metrics that may be of interest (Figure 5B last two rows): overall spike size (amplitude; trough-to-peak magnitude) and recording position (estimated depth). N1 waveforms had the largest mean amplitude of all other classes ($p < 0.011$), signifying that N1 may represent recordings from large neurons or recordings of cells that were near the electrode (Holt & Koch, 1999; Gold *et al.*, 2006). In terms of the anatomical recording positions, three out of the four classical negative-spiking classes (N2, B1, and B2) were recorded significantly deeper than the positive-spiking and triphasic classes (T, P1, and P2) ($p < 0.023$). The more superficial position of positive and triphasic units suggests they were from thalamocortical or corticothalamic axonal fibers traveling to or from the LGN, with thalamocortical projections being more frequent due to the significantly faster response latencies of the positive-spiking groups.

Just as the RF population depended on methodological factors (Figure 4D), the proportion of waveform type also depended on electrode type and stimulus type (Figure 5C top). When comparing the proportion of waveform units obtained from multi- or single-channeled electrodes, nearly all (96%, $n = 46/48$) of the single-channel data were negative-

spiking units (N1, N2, B1, B2) with only 2% of the single-channel population to each of positive (n = 1/48) and triphasic units (n = 1/48). Out of the negative classes, the single-channel electrodes recorded no N1 spiking units and a large portion of broad-spiking units (75%: B1, 31%; B2, 44%), which may be due to the dissimilar electrode properties or selection bias for strong signals when using single-channel electrodes as opposed to multi-channel electrodes (Talebi & Baker, 2016). Expanding on this idea, the negative-voltage threshold commonly used when searching for neurons might have biased the single-channel population. This effect would have been lessened by the multi-channel electrodes that were optimized for only one channel if at all, and thus, any fine positioning bias that might be present on one channel would not be present for the other channels. Furthermore, like with the dependency between stimulus type and RF type, the 21% increase in positive-spiking units in the higher contrast and coarse stimuli than in the fine stimuli (47% versus 26%) suggests there is also a dependency between stimulus type and recorded waveform types.

Discussion

Extracellular spike waveforms

In the negative-dominant waveform classes (N1, N2, B1, B2), the negative and positive phases are generated by the opening and closing of sodium and potassium channels, respectively. These typical extracellular waveforms occur when the recording contact is near the neuron's soma with minimal influence from other structures (Holt & Koch, 1999; Gold *et al.*, 2006). These classes are differentiated by spike duration, with broad waveforms loosely linked to excitatory neurons and narrow waveforms to inhibitory neurons (Henze *et al.*, 2000;

Barthó *et al.*, 2004; Sukman & Stark, 2022). We have not made this assumption for our dataset because excitatory cells have exhibited narrow-spiking extracellular waveforms (Vigneswaran *et al.*, 2011), and inhibitory interneurons in mouse cortex have exhibited broad-spiking waveforms, intracellularly (Gentet *et al.*, 2010).

The upward deflection in triphasic- and positive-spiking waveforms has been described as the mixed-ion capacitive current from surrounding sources for recordings distal to the soma as the spike propagates through an isolated unmyelinated axon (Clark & Plonsey, 1968; Raastad & Shepherd, 2003; Heinricher, 2004; Gold *et al.*, 2006; Lewandowska *et al.*, 2015). Furthermore, previous studies have shown that only triphasic- and positive-spiking waveforms were recorded from silenced brain regions (Barry, 2015; Sun *et al.*, 2021; Sibille *et al.*, 2022), demonstrating that these waveforms are of afferent fibers originating from previous processing areas. Our findings are consistent with these reports, as the positive waveforms (P1, P2), and to a lesser extent the triphasic waveforms (T), had shorter response latencies than the negative-spiking classes, suggesting they reflect axonal fibers of passage of retinal ganglion cells.

Although the waveform clustering algorithm used here provided well-defined waveform groupings, there were multiple variations within each waveform class. Within the negative classes, a small population were doublet-spiking waveforms that may reflect retinal spikes impinging on LGN neurons (S-potentials: Sincich *et al.*, 2007), or intermediate LGN neurons like those found in ferret LGN (Murphy *et al.*, 2020). Within the positive classes, we noticed several M-shaped waveforms (double positive peaks), which could also be from S-potentials or from distal neuronal activity such as from dendrites (Holt & Koch, 1999; Gold *et al.*, 2006). Due to their rarity, we did not investigate if these unusual waveforms functionally differed from others. Such subpopulations are rarely reported in the literature

and may require substantially higher sampling counts in order to understand the full extent of extracellular action potentials and associated functional classes.

RF classification

Although we based our RF classification on previous LGN studies (Wiesel & Hubel, 1966; Reid & Shapley, 2002), we made an adjustment in RF classification: for a response to be considered P, both opposing *L*- and *M*-cones had to be significantly above noise. This is because, when classifying our RFs using the traditional method (sign only), we found several RFs that qualitatively appeared to be magnocellular, but would have been labeled parvocellular by classical criteria due to *L*- or *M*-cone responses within the noise floor, resulting in an inaccurate sign (see Extended Figure 3-2 for examples). Our new classification is more robust in the face of experimental uncertainty while preserving the functional definitions.

Correlations

We have reported distinct correlations between extracellular spike shape and RF characteristics. First, the narrow-spiking classes (N1 and N2) had a 1.5-to-1 ratio of P-to-M RFs, as often seen in LGN extracellular recordings (Pietersen *et al.*, 2014). Even though this ratio is much lower than the 8-to-1 ratio of the parvocellular-to-magnocellular population in the LGN (Prasad & Galetta, 2011), the extracellular ratio is likely due to a sampling bias of extracellular recordings towards the larger magnocellular neurons ("the larger the fish, the higher the probability of a hit" — Towe & Harding, 1970).

Second, positive-spiking waveforms (P1 and P2) had a 1-to-4 ratio of P-to-M RFs. Suppose we assume positive spikes are afferent axons from the retina, and the LGN has a 1-to-1 ratio to retinal ganglion cell input (Spear et al., 1996); why are the ratios of RF classes in the positive and negative classes unequal? One might assume that negative and positive spikes are functionally different, but we think that sampling biases were involved when recording from axonal activity. Notably, the generally larger sized axons of parasol/magnocellular than midget/parvocellular and koniocellular (Walsh *et al.*, 2000), the larger magnocellular-to-parvocellular ratio as eccentricity increases (Livingstone & Hubel, 1988), the degree of axon myelination (Holt & Koch, 1999), or the prevalence of magnocellular LGN axons as they course through the interior of the area toward the primary visual cortex, all of which would have likely to have biased our axonal (positive spikes) population towards magnocellular recordings.

Third, N RFs (those without an estimated RF) were found with higher proportion in the broad-spiking waveform classes (B1 and B2) compared to all other waveform classes. We observed that N RFs had many response characteristics that differed from units with an estimated RF (discussed further below).

Non-RF units

N units pose an interesting question regarding visual processing: what are they, and why are they being recorded? We found that half of N units responded reliably to the stimulus (59%) albeit at a reduced spike and burst rate than RF units. The shortage in spiking activity could be from the electrode channels losing contact with the source, which may explain the high proportion of N units in the broad-spiking population, as contact distance is proportional to spike waveform width (Gold *et al.*, 2006). The shortage of burst activity for N units may be

associated with a lack of stimulus contrast processing (Sanchez *et al.*, 2023), higher label information processing (Butts *et al.*, 2010), or a lack of retinothalamic transmission of visual information (Alitto *et al.*, 2019). Together, this evidence from the literature can suggest that N units may have been corticothalamic projections, such as those that influence response gain (Murphy *et al.*, 2021).

For the remaining N units that did not reliably respond to the stimulus (43%), what do these units do if they are not being visually stimulated? As here, Vries *et al.* (2020) found 23% of mouse visual cortex neurons (~60,000 total) did not reliably respond to visual stimuli, with the proportion of non-responsive units increasing in higher visual areas. They speculated that these units might be involved in specific natural features from hierarchical processing, modulated by multimodal senses (Stringer *et al.*, 2019), or non-visual computation, such as motion, identified in the dLGN of mice (Orlowska-Feuer *et al.*, 2022), which can all be true for our N units. It is also possible that these N units may explain the retinal ganglion cell classes projecting to the LGN that are not associated with classic thalamic responses (~20%: Dacey, 2004). While it may be simply that there was insufficient activity for a significant LGN RF to be recovered, gaining insight into non-responsive units in future studies is integral to a fuller understanding of visual processing (Olshausen & Field, 2005).

Evidence for recording bias

Differences in populations between the multi-channel and single-channel recordings is likely due to sampling bias. Talebi & Baker (2016) postulated that manually controlled single-channel electrodes in combination with a search stimulus to identify responsive neurons, largely avoided in our multi-channel recordings, creates a selection bias toward user-preferred neurons. Similarly, we believe that previous studies using single-channel electrodes

may have passed over the atypical positive-spiking units when searching for neurons, especially when using a negative trigger threshold when searching for neurons or during off-line spike-sorting.

It is important to note that the current study should be viewed as a partial survey of the LGN, rather than an exhaustive one. We searched while listening for spikes along with looking for them, often using a negative trigger threshold. This strategy may have created a selection bias despite our attempts to mitigate those effects, and the true proportion of positive-spiking waveforms may be higher than what we have reported. For example, Paulk *et al.* (2022) recorded more positive-spiking than negative-spiking units in human cortex using dense multi-channel electrodes. Several other experimental biases are difficult to avoid in extracellular recordings, such as preference for large extracellular action potentials, units with high firing rates, or units that are visually responsive to the stimulus (Olshausen & Field, 2005). Thus, future studies need to consider the possible biases when recording extracellularly and, in effect, the difficulties involved in obtaining a completely objective study of a neuronal population.

Conclusion

Here, we report seven extracellular spike waveform classes in the LGN, each composed of distinct receptive field and spiking dynamics. We observed several types of units that have not been regularly documented before, like the non-RF units that consistently responded to the visually presented noise stimulus but at a low and sustained response rate, indicating they may be a class that has yet to be identified. Our observations suggest that the neuronal classifications in the LGN may be more numerous than traditionally held, and a fully developed understanding of the complexities of LGN may require nuances beyond the

classical division into M, P, and K responses, nuances that could reveal previously undiscovered, sophisticated computations in the visual system.

References

Alitto H, Rathbun DL, Vandeleest JJ, Alexander PC & Usrey WM (2019). The Augmentation of Retinogeniculate Communication during Thalamic Burst Mode. *J Neurosci* **39,** 5697–5710.

Barry JM (2015). Axonal activity in vivo: technical considerations and implications for the exploration of neural circuits in freely moving animals. *Front Neurosci*; DOI: 10.3389/fnins.2015.00153.

Barthó P, Hirase H, Monconduit L, Zugaro M, Harris KD & Buzsáki G (2004). Characterization of Neocortical Principal Cells and Interneurons by Network Interactions and Extracellular Features. *J Neurophysiol* **92,** 600–608.

Blondel VD, Guillaume J-L, Lambiotte R & Lefebvre E (2008). Fast unfolding of communities in large networks. *J Stat Mech Theory Exp* **2008,** P10008.

Butts DA, Desbordes G, Weng C, Jin J, Alonso J-M & Stanley GB (2010). The Episodic Nature of Spike Trains in the Early Visual Pathway. *J Neurophysiol* **104,** 3371–3387.

Callaway EM (2005). Structure and function of parallel pathways in the primate early visual system: Structure and function of parallel visual pathways. *J Physiol* **566,** 13–19.

Clark J & Plonsey R (1968). The Extracellular Potential Field of the Single Active Nerve Fiber in a Volume Conductor. *Biophys J* **8,** 842–864.

Dacey D (2004). Origins of perception: Retinal Ganglion Cell Diversity and the Creation of Parallel Visual Pathways. In *Sensory Systems*, pp. 281–301.

De Monasterio FM & Gouras P (1975). Functional properties of ganglion cells of the rhesus monkey retina. *J Physiol* **251,** 167–195.

De Monasterio FM, Gouras P & Tolhurst DJ (1975). Trichromatic colour opponency in ganglion cells of the rhesus monkey retina. *J Physiol* **251,** 197–216.

Derrington AM, Krauskopf J & Lennie P (1984). Chromatic mechanisms in lateral geniculate nucleus of macaque. *J Physiol* **357,** 241–265.

Derrington AM & Lennie P (1984). Spatial and temporal contrast sensitivities of neurones in lateral geniculate nucleus of macaque. *J Physiol* **357,** 219–240.

Eiber CD, Rahman AS, Pietersen ANJ, Zeater N, Dreher B, Solomon SG & Martin PR (2018). Receptive Field Properties of Koniocellular On/Off Neurons in the Lateral Geniculate Nucleus of Marmoset Monkeys. *J Neurosci* **38,** 10384–10398.

Gentet LJ, Avermann M, Matyas F, Staiger JF & Petersen CCH (2010). Membrane Potential Dynamics of GABAergic Neurons in the Barrel Cortex of Behaving Mice. *Neuron* **65,** 422–435.

Gold C, Girardin CC, Martin KAC & Koch C (2009). High-Amplitude Positive Spikes Recorded Extracellularly in Cat Visual Cortex. *J Neurophysiol* **102,** 3340–3351.

Gold C, Henze DA, Koch C & Buzsáki G (2006). On the Origin of the Extracellular Action Potential Waveform: A Modeling Study. *J Neurophysiol* **95,** 3113–3128.

Heinricher MM (2004). Principles of extracellular single-unit recording. *Microelectrode Rec Mov Disord Surg*.

Henze DA, Borhegyi Z, Csicsvari J, Mamiya A, Harris KD & Buzsáki G (2000). Intracellular Features Predicted by Extracellular Recordings in the Hippocampus In Vivo. *J Neurophysiol* **84,** 390–400.

Holt GR & Koch C (1999). Electrical Interactions via the Extracellular Potential Near Cell Bodies. *J Comput Neurosci* **6,** 169–184.

Horwitz GD & Albright TD (2005). Paucity of chromatic linear motion detectors in macaque V1. *J Vis* **5,** 4.

Horwitz GD, Chichilnisky EJ & Albright TD (2007). Cone Inputs to Simple and Complex Cells in V1 of Awake Macaque. *J Neurophysiol* **97,** 3070–3081.

Hubel DH & Livingstone MS (1990). Color and contrast sensitivity in the lateral geniculate body and primary visual cortex of the macaque monkey. *J Neurosci* **10,** 2223–2237.

Kaplan E & Shapley RM (1982). X and Y cells in the lateral geniculate nucleus of macaque monkeys. *J Physiol* **330,** 125–143.

Killian NJ, Vurro M, Keith SB, Kyada MJ & Pezaris JS (2016). Perceptual learning in a non-human primate model of artificial vision. *Sci Rep* **6,** 1–16.

Lee EK, Balasubramanian H, Tsolias A, Anakwe SU, Medalla M, Shenoy KV & Chandrasekaran C (2021). Non-linear dimensionality reduction on extracellular waveforms reveals cell type diversity in premotor cortex ed. Salinas E & Frank MJ. *eLife* **10,** e67490.

Lewandowska MK, Bakkum DJ, Rompani SB & Hierlemann A (2015). Recording Large Extracellular Spikes in Microchannels along Many Axonal Sites from Individual Neurons ed. Martinoia S. *PLOS ONE* **10,** e0118514.

Livingstone MS & Hubel DH (1988). Do the relative mapping densities of the magno- and parvocellular systems vary with eccentricity? *J Neurosci* **8,** 4334–4339.

Martin PR & Lee BB (2014). Distribution and specificity of S-cone (“blue cone”) signals in subcortical visual pathways. *Vis Neurosci* **31,** 177–187.

Maunsell JHR, Ghose GM, Assad JA, McADAMS CJ, Boudreau CE & Noerager BD (1999). Visual response latencies of magnocellular and parvocellular LGN neurons in macaque monkeys. *Vis Neurosci* **16,** 1–14.

McInnes L, Healy J & Melville J (2020). UMAP: Uniform Manifold Approximation and Projection for Dimension Reduction. *ArXiv180203426 Cs Stat*. Available at: http://arxiv.org/abs/1802.03426 [Accessed May 1, 2022].

Meeks JP, Jiang X & Mennerick S (2005). Action potential fidelity during normal and epileptiform activity in paired soma–axon recordings from rat hippocampus. *J Physiol* **566,** 425–441.

Murphy AJ, Hasse JM & Briggs F (2020). Physiological characterization of a rare subpopulation of doublet-spiking neurons in the ferret lateral geniculate nucleus. *J Neurophysiol* **124,** 432–442.

Murphy AJ, Shaw L, Hasse JM, Goris RLT & Briggs F (2021). Optogenetic activation of corticogeniculate feedback stabilizes response gain and increases information coding in LGN neurons. *J Comput Neurosci* **49,** 259–271.

Olshausen BA & Field DJ (2005). How Close Are We to Understanding V1? *Neural Comput* **17,** 1665–1699.

Orlowska-Feuer P, Ebrahimi AS, Zippo AG, Petersen RS, Lucas RJ & Storchi R (2022). Look-up and look-down neurons in the mouse visual thalamus during freely moving exploration. *bioRxiv*.

Pachitariu M, Steinmetz N, Kadir S, Carandini M & Harris KD (2016). Kilosort: realtime spike-sorting for extracellular electrophysiology with hundreds of channels. ; DOI: 10.1101/061481.

Paulk AC, Kfir Y, Khanna AR, Mustroph ML, Trautmann EM, Soper DJ, Stavisky SD, Welkenhuysen M, Dutta B, Shenoy KV, Hochberg LR, Richardson RM, Williams ZM & Cash SS (2022). Large-scale neural recordings with single neuron resolution using Neuropixels probes in human cortex. *Nat Neurosci* **25,** 252–263.

Pietersen ANJ, Cheong SK, Munn B, Gong P, Martin PR & Solomon SG (2017). Relationship between cortical state and spiking activity in the lateral geniculate nucleus of marmosets. *J Physiol* **595,** 4475–4492.

Pietersen ANJ, Cheong SK, Solomon SG, Tailby C & Martin PR (2014). Temporal response properties of koniocellular (blue-on and blue-off) cells in marmoset lateral geniculate nucleus. *J Neurophysiol* **112,** 1421–1438.

Prasad S & Galetta SL (2011). Anatomy and physiology of the afferent visual system. In *Handbook of Clinical Neurology*, pp. 3–19. Elsevier. Available at: https://linkinghub.elsevier.com/retrieve/pii/B9780444529039000078 [Accessed July 11, 2022].

Raastad M & Shepherd GMG (2003). Single-axon action potentials in the rat hippocampal cortex. *J Physiol* **548,** 745–752.

Reid RC & Shapley RM (2002). Space and Time Maps of Cone Photoreceptor Signals in Macaque Lateral Geniculate Nucleus. *J Neurosci* **22,** 6158–6175.

Rossant C, Kadir SN, Goodman DFM, Schulman J, Hunter MLD, Saleem AB, Grosmark A, Belluscio M, Denfield GH, Ecker AS, Tolias AS, Solomon S, Buzsáki G, Carandini M & Harris KD (2016). Spike sorting for large, dense electrode arrays. *Nat Neurosci* **19,** 634–641.

Ruiz O, Royal D, Sáry G, Chen X, Schall JD & Casagrande VA (2006). Low-Threshold Ca2+-Associated Bursts Are Rare Events in the LGN of the Awake Behaving Monkey. *J Neurophysiol* **95,** 3401–3413.

Sanchez AN, Alitto HJ, Rathbun DL, Fisher TG & Usrey WM (2023). Stimulus contrast modulates burst activity in the lateral geniculate nucleus. *Curr Res Neurobiol* **4,** 100096.

Schiller PH & Malpeli JG (1978). Functional specificity of lateral geniculate nucleus laminae of the rhesus monkey. *J Neurophysiol* **41,** 788–797.

Schwartz O, Pillow JW, Rust NC & Simoncelli EP (2006). Spike-triggered neural characterization. *J Vis* **6,** 13.

Sharpee TO (2013). Computational Identification of Receptive Fields. *Annu Rev Neurosci* **36,** 103–120.

Sherman SM (2001). Tonic and burst firing: dual modes of thalamocortical relay. *Trends Neurosci* **24,** 122–126.

Sherman SM & Guillery RW (2006). *Exploring the thalamus and its role in cortical function, 2nd ed*. MIT Press, Cambridge, MA, US.

Sibille J, Gehr C, Benichov JI, Balasubramanian H, Teh KL, Lupashina T, Vallentin D & Kremkow J (2022). High-density electrode recordings reveal strong and specific connections between retinal ganglion cells and midbrain neurons. *Nat Commun* **13,** 5218.

Simoncelli EP & Olshausen BA (2001). Natural Image Statistics and Neural Representation. *Annu Rev Neurosci* **24,** 1193–1216.

Sincich LC, Adams DL, Economides JR & Horton JC (2007). Transmission of Spike Trains at the Retinogeniculate Synapse. *J Neurosci* **27,** 2683–2692.

Solomon SG & Lennie P (2007). The machinery of colour vision. *Nat Rev Neurosci* **8,** 276–286.

Stockman A & Sharpe LT (2000). The spectral sensitivities of the middle- and long-wavelength-sensitive cones derived from measurements in observers of known genotype. *Vision Res* **40,** 1711–1737.

Stringer C, Pachitariu M, Steinmetz N, Reddy CB, Carandini M & Harris KD (2019). Spontaneous behaviors drive multidimensional, brainwide activity. *Science*; DOI: 10.1126/science.aav7893.

Sukman LJ & Stark E (2022). Cortical Pyramidal and Parvalbumin Cells Exhibit Distinct Spatiotemporal Extracellular Electric Potentials. *eNeuro*; DOI: 10.1523/ENEURO.0265-22.2022.

Sun H, Smithson HE, Zaidi Q & Lee BB (2006). Specificity of Cone Inputs to Macaque Retinal Ganglion Cells. *J Neurophysiol* **95,** 837–849.

Sun SH, Almasi A, Yunzab M, Zehra S, Hicks DG, Kameneva T, Ibbotson MR & Meffin H (2021). Analysis of extracellular spike waveforms and associated receptive fields of neurons in cat primary visual cortex. *J Physiol* **599,** 2211–2238.

Tailby C, Szmajda BA, Buzás P, Lee BB & Martin PR (2008). Transmission of blue (S) cone signals through the primate lateral geniculate nucleus: Spatial properties of S-cone pathways. *J Physiol* **586,** 5947–5967.

Talebi V & Baker CL (2016). Categorically distinct types of receptive fields in early visual cortex. *J Neurophysiol* **115,** 2556–2576.

Towe AL & Harding GW (1970). Extracellular microelectrode sampling bias. *Exp Neurol* **29,** 366–381.

Usrey WM & Reid RC (2000). Visual physiology of the lateral geniculate nucleus in two species of New World monkey: Saimiri sciureus and Aotus trivirgatis. *J Physiol* **523,** 755–769.

Vigneswaran G, Kraskov A & Lemon RN (2011). Large Identified Pyramidal Cells in Macaque Motor and Premotor Cortex Exhibit “Thin Spikes”: Implications for Cell Type Classification. *J Neurosci* **31,** 14235–14242.

Vries SEJ de et al. (2020). A large-scale standardized physiological survey reveals functional organization of the mouse visual cortex. *Nat Neurosci* **23,** 138–151.

Walsh N, Ghosh KK & FitzGibbon T (2000). Intraretinal axon diameters of a New World primate, the marmoset (Callithrix jacchus). *Clin Experiment Ophthalmol* **28,** 423–430.

Wang W, Jones HE, Andolina IM, Salt TE & Sillito AM (2006). Functional alignment of feedback effects from visual cortex to thalamus. *Nat Neurosci* **9,** 1330.

White AJR, Solomon SG & Martin PR (2001). Spatial properties of koniocellular cells in the lateral geniculate nucleus of the marmoset Callithrix jacchus. *J Physiol* **533,** 519–535.

White AJR, Wilder HD, Goodchild AK, Sefton AJ & Martin PR (1998). Segregation of Receptive Field Properties in the Lateral Geniculate Nucleus of a New-World Monkey, the Marmoset Callithrix jacchus. *J Neurophysiol* **80,** 2063–2076.

Wiesel TN & Hubel DH (1966). Spatial and chromatic interactions in the lateral geniculate body of the rhesus monkey. *J Neurophysiol* **29,** 1115–1156.

Figures

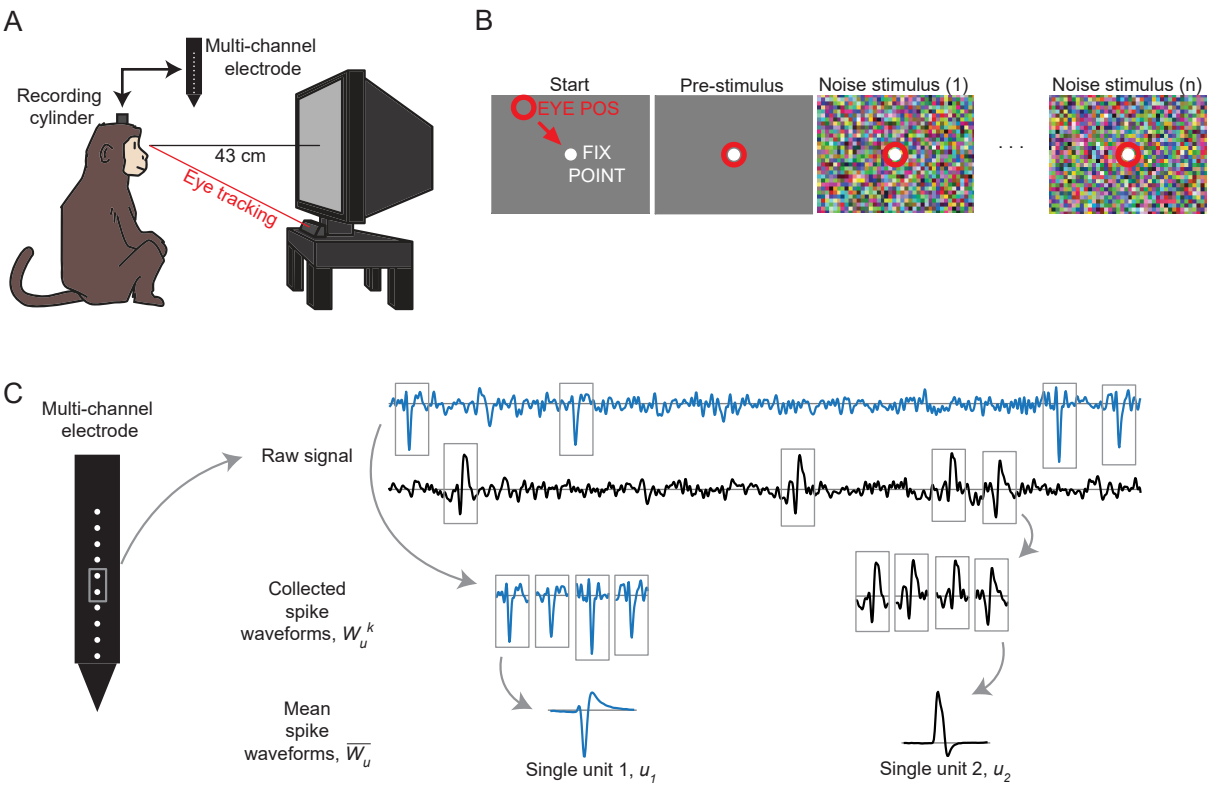

Figure 1. Experimental design. **(A)** Animals were placed in front of a CRT monitor, with neutral gaze position near the center of the monitor. Gaze location was monitored through an infrared eye tracker. Multi-channel electrodes were inserted through surgically-implanted titanium recording cylinders which maintained chronic access to the dura. **(B)** The trial-based mapping task. The animal was required to fixate on a small spot in the center of the screen for 0.4 sec, before the mapping stimulus commenced, and to maintain fixation on the spot for the duration of the mapping stimulus. Mapping stimuli were presented for 2.5 to 5.0 seconds. **(C)** Schematic of extracellular spike waveform extraction. For each single unit (u), spike waveforms were extracted from the raw signal (W_u^k) in 4.5 ms windows and then averaged to obtain the mean waveform ($\overline{W_u}$).

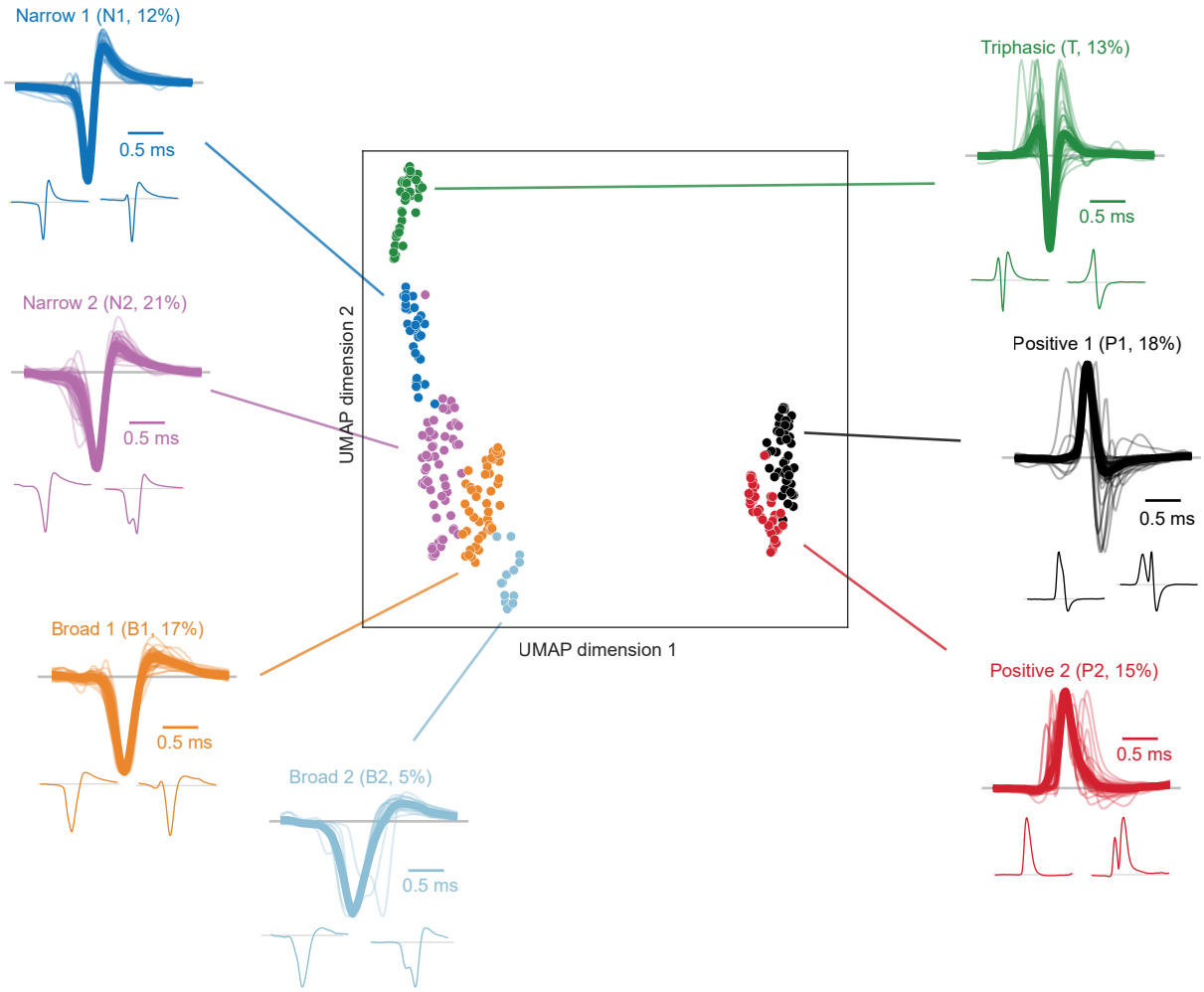

Figure 2. Extracellular mean spike waveforms are classified using WaveMAP (Lee *et al.*, 2021). In the middle, scatter plot visualization of each single unit's mean spike waveform in UMAP space, where the horizontal and vertical axes represent the dimension-reduced UMAP coefficients. The data points are colored by the seven waveform classifications from WaveMAP: *Narrow 1* (N1, blue); *Narrow 2* (N2, purple); *Broad 1* (B1, orange); *Broad 2* (B2, light blue); *Triphasic* (T, green); *Positive 1* (P1, black); and *Positive 2* (P2, red). Surrounding the scatter plot are the mean spike waveform traces for each single unit (light lines) with the group mean waveform overlayed on top (dark and bold lines), for each class of waveforms. Negative-spiking groups are normalized to the negative peak, and positive-spiking classes (P1 and P2) are normalized to the positive peak. The smaller individual waveforms illustrated below the grouped waveforms are two examples to show the variation

within each class. Gray lines within the illustrated waveforms represent baseline voltage. All waveforms were plotted within a 2.5 ms window. See Extended Figure 2-1 for illustrations of all extracellular spike waveforms.

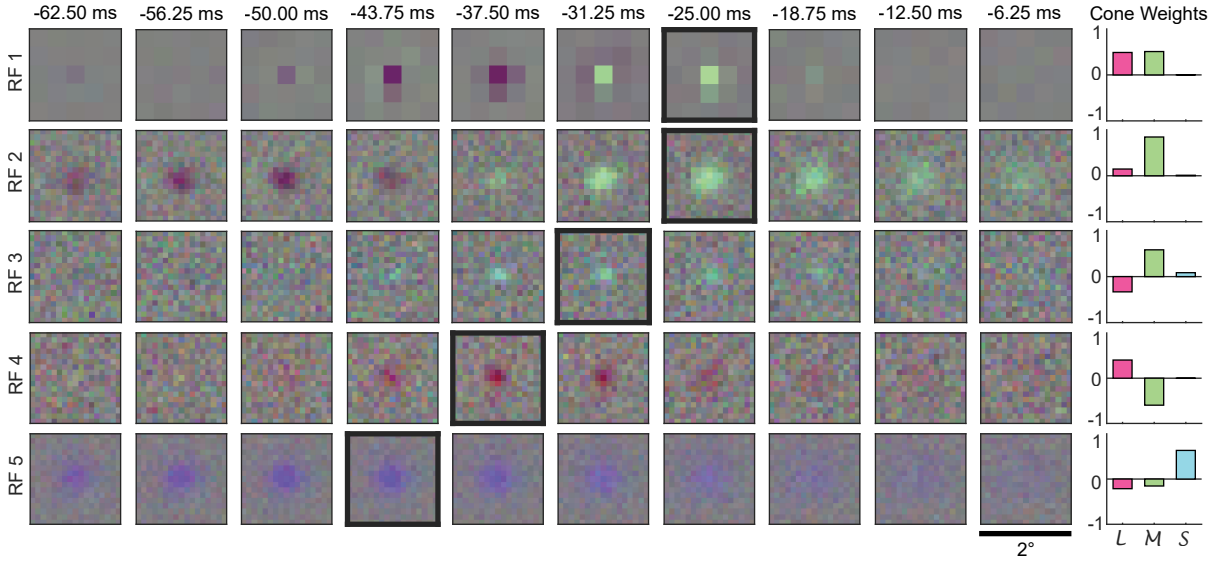

Figure 3. Five example chromospatiotemporal receptive fields (RFs), one per row, spanning 12 stimulus frames, one per 6.25 ms. RF 1 was measured using coarse-resolution stimuli, and RF 2–5 were measured using fine-resolution stimuli. All plots span 2.0° of the visual field. Bolded black outlines indicate the frame in an RF with the largest magnitude (RF_{max}). On the right are the cone weights for each example, indicated as long- (L, magenta), medium- (M, green), and short-cone wavelengths (S, blue) on the x-axis and the normalized response on the y-axis. See Extended Figure 3-2 for the RF_{max} and cone weights for all RF units.

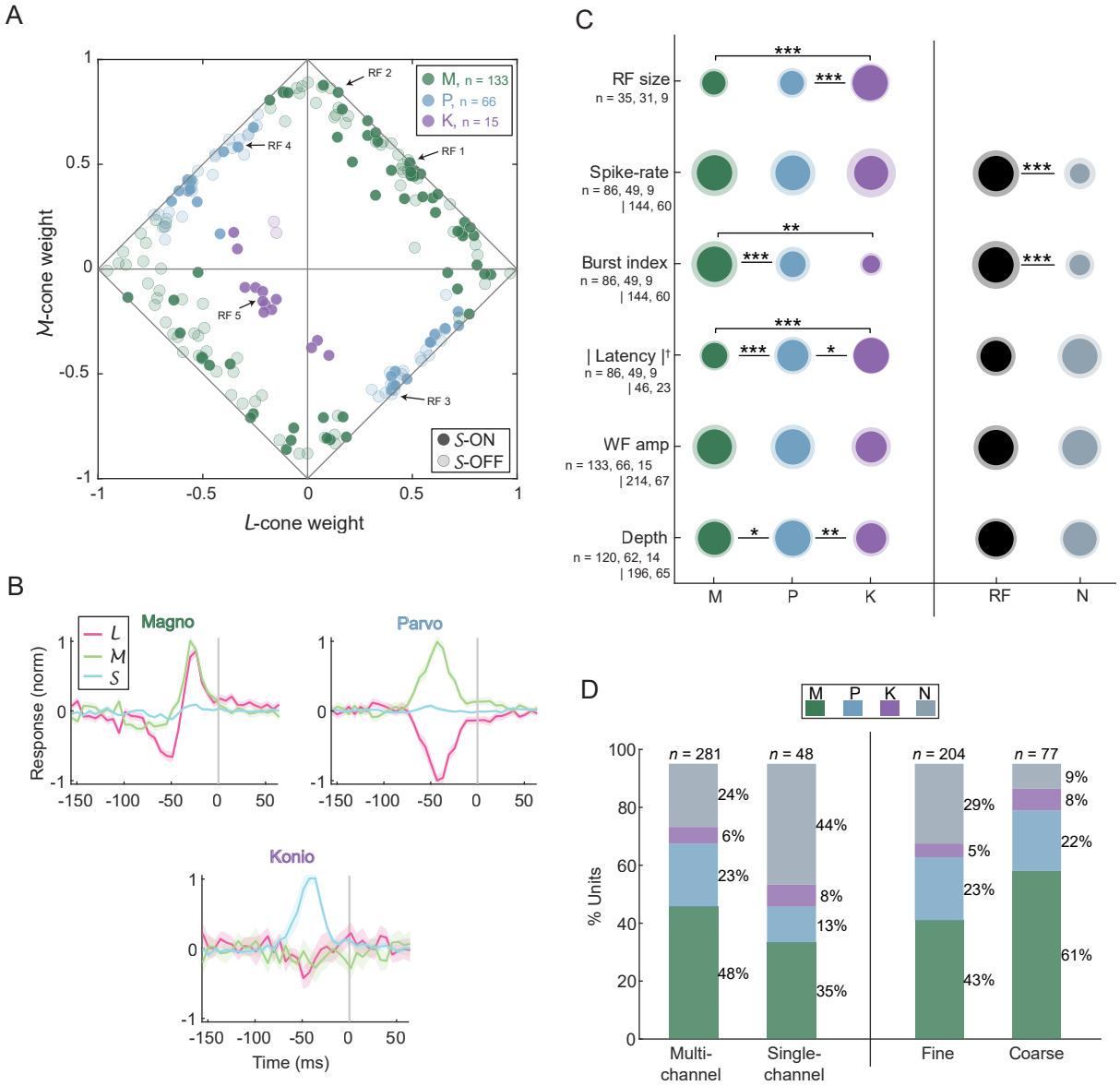

Figure 4. Receptive field classification and analysis (n = 197). **(A)** Normalized cone weights ($|L| + |M| + |S| = 1$) for all RFs plotted on the LM plane. The horizontal and vertical axes represent L- and M-cone weights, respectively. The magnitude of the S-cone weight is represented as the distance from the diamond lines. The circular and diamond-shaped data points with positive and negative S-cone weights, respectively. The data points colored in green, light-blue, and purple represent magnocellular (M), parvocellular (P), and koniocellular (K) RFs, respectively (also in subplots C and D). **(B)** Mean temporal weighting functions (TWFs), describing the average cone response over time for M (top-left), P (top-

right), and K (bottom) RFs. The grey line indicates spike onset. For M and K RFs, weighting functions were multiplied by –1 for *off* RFs, and for P RFs, responses were flipped if the maximum L-cone response was negative. **(C)** Intensity visualization summarizing the mean value of a response metric for each RF class separated into M, P, and K on the left and RF and non-RF (N) units on the right. The area of the inner and outer circles represents the mean and standard deviation, respectively. The notations *, ** and *** represent $p < 0.05$, $p < 0.01$ and $p < 0.001$ (unpaired t-test), respectively. Note that response latency (indicated by the dagger symbol, †) was calculated differently for the left (from the RF_{max}) and right datasets (from the PSTH). Since differences in stimulus statistics have been known to affect spiking metrics (Almasi *et al.*, 2022; Sanchez *et al.*, 2023), the RF size, spike-rate, burst index, and response latency mentioned in this and following sections were from units stimulated with fine-stimulus only. |Latency| refers to the absolute response latency. **(D)** Percentage of units recorded from multi-channel electrodes versus single-channel electrodes (left) and units recorded with the fine stimuli versus coarse stimuli (right) for each RF class.

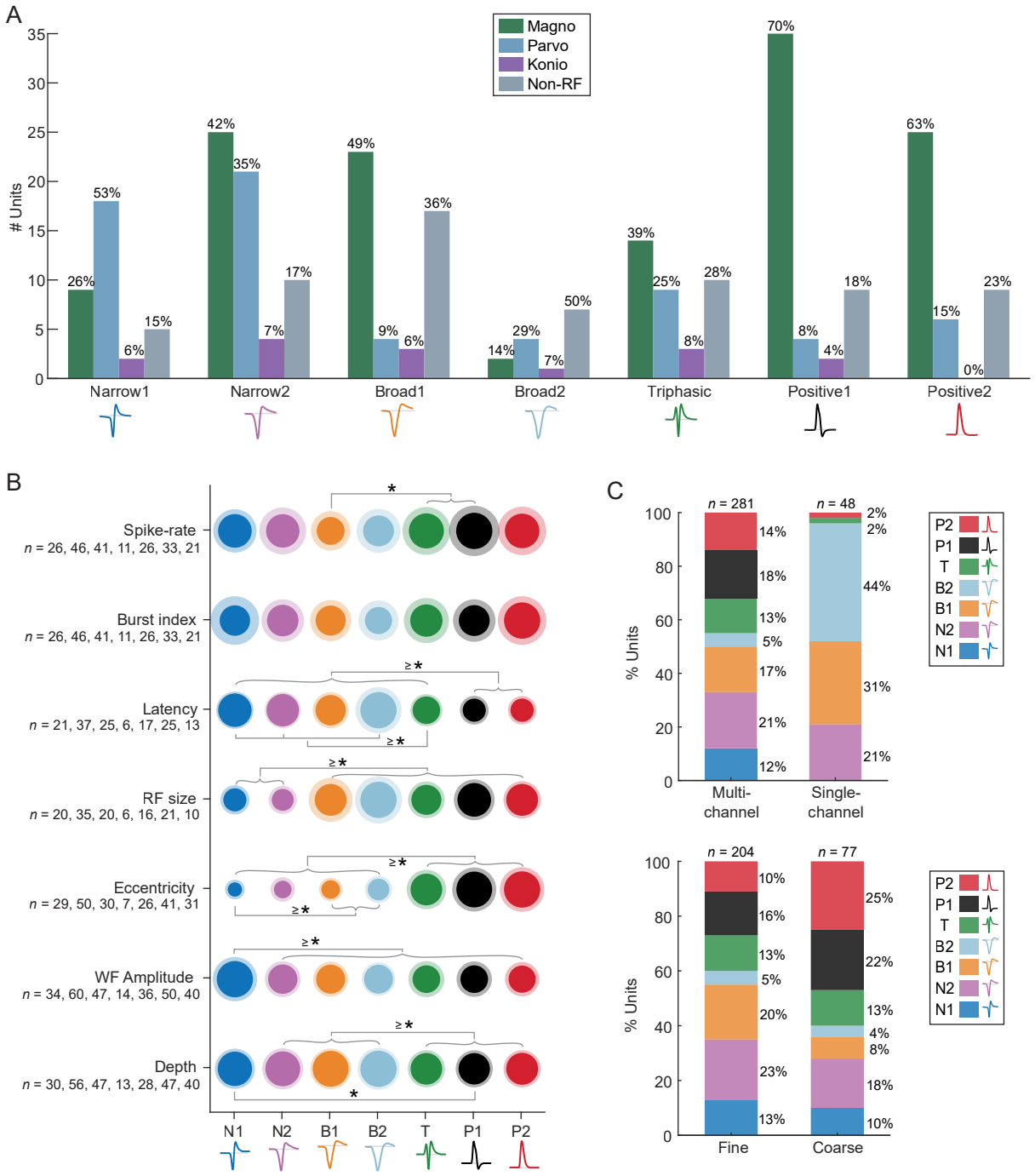

Figure 5. Correlations and analyses of spike waveform classes against RF classes and response characteristics. **(A)** Bar plot of waveform class population to their RF type (M, P, K, N) as number of units (n = 281). The percentage above each bar indicates the proportion of each RF type within that waveform class. **(B)** Intensity visualization summarizing the mean value of a response metric for each waveform class, like in Figure 4C. The area of the inner and outer circles represents the mean and standard deviation, respectively. The notations *,

** and *** represent $p < 0.05$, $p < 0.01$ and $p < 0.001$ (unpaired *t*-test), respectively. RF population for each dataset is stated below each tick label along the vertical axis. Spike-rate, burst index, latency, and RF size were estimated from units presented with fine-stimuli. **(C)** The percentage of units recorded from multi-channel versus single-channel electrodes for each spike waveform class. The percentages on the right of each bar denote the proportion of each waveform class, and the number above denotes the total number of units within that bar.

SUPPLEMENTARY MATERIAL

Appendix S1: Glossary

SU, single unit: isolated extracellular recording from an individual neuron.

CSTRF, chromospatiotemporal receptive field: the receptive field of an LGN cell measured across color and visual spaces, and through time.

RF, receptive field: the response of the optimal stimulus for a given cell, used interchangeably with the CSTRF.

RF unit: a single unit with a significant receptive field.

STA, spike triggered average: the averaged stimulus image conditioned on spike time, here used to calculate the CSTRF.

R, G, B; red, green, blue: the three phosphor colors used in computer monitors and, here, to generate visual stimuli.

Lum, luminance matrix: determined by the magnitude of the colored phosphors.

$RF_{location}$: the location of CSTRF with the maximum, from *Lum*, in *x*-space, *y*-space, and time.

RF position: the *x* and *y* spatial components of $RF_{location}$.

RF latency: the temporal component of $RF_{location}$.

RF_{max}: the spatial plane at RF latency.

Lum_{max}: the luminance matrix of RF_{max}.

RF_{noise}: the acausal frames of the CSTRF.

η: noise in a signal; used to select RFs with significant amplitudes.

L, M, S; long, medium, short: retinal photoreceptor cones classified by wavelength of peak sensitivity.

M, magnocellular: RFs with contribution from L- and M-cone weights that were non-opposing.

P, parvocellular: RFs with contribution from L- and M-cone weights that were opposing and significantly above noise.

K, koniocellular: RFs with the largest contribution from S-cone.

N, non-RF unit: cells that do not have significant receptive fields.

TWF, temporal weighting function: the LMS response of a given pixel, or average pixel, over time.

Narrow 1, 2: narrow, negative-going spike waveform classifications (see Fig. 2).

Broad 1, 2: broad, negative-going spike waveform classifications (see Fig. 2).

Triphasic: negative-going spike waveform classification but typically with an addition of an initial positive deflection (see Fig. 2).

Positive 1, 2: positive-going spike waveform classifications (see Fig. 2).

Coarse stimulus: 80 x 60 colored noise stimulus (see Extended Fig. 1-1).

Fine stimulus: 400 x 300 colored noise stimulus (see Extended Fig. 1-1).

Extended Figures

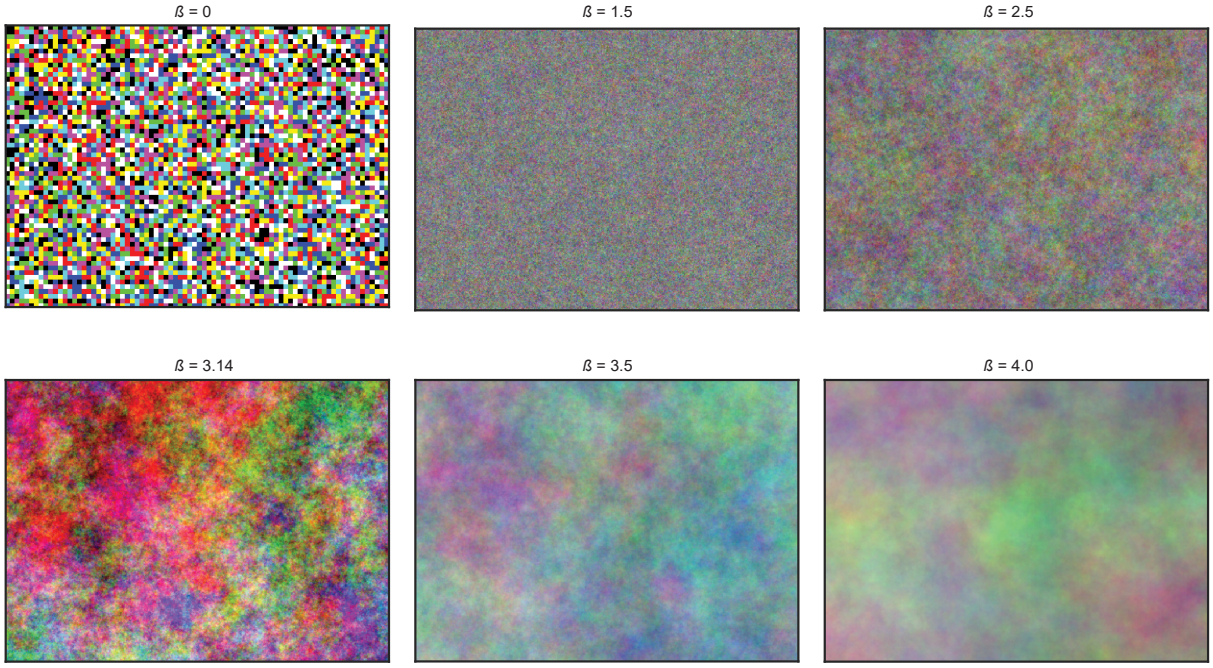

Figure 1-1. Example images from six different stimulus sets. The first is the 80 by 60 coarse-resolution stimulus with a white power spectrum ($\beta = 0$). The remaining are stimulus sets using fine-resolution 400 by 300 pixel images with varying power spectra ($\beta = 1.5$, 2.5, 3.14, 3.5, or 4.0).

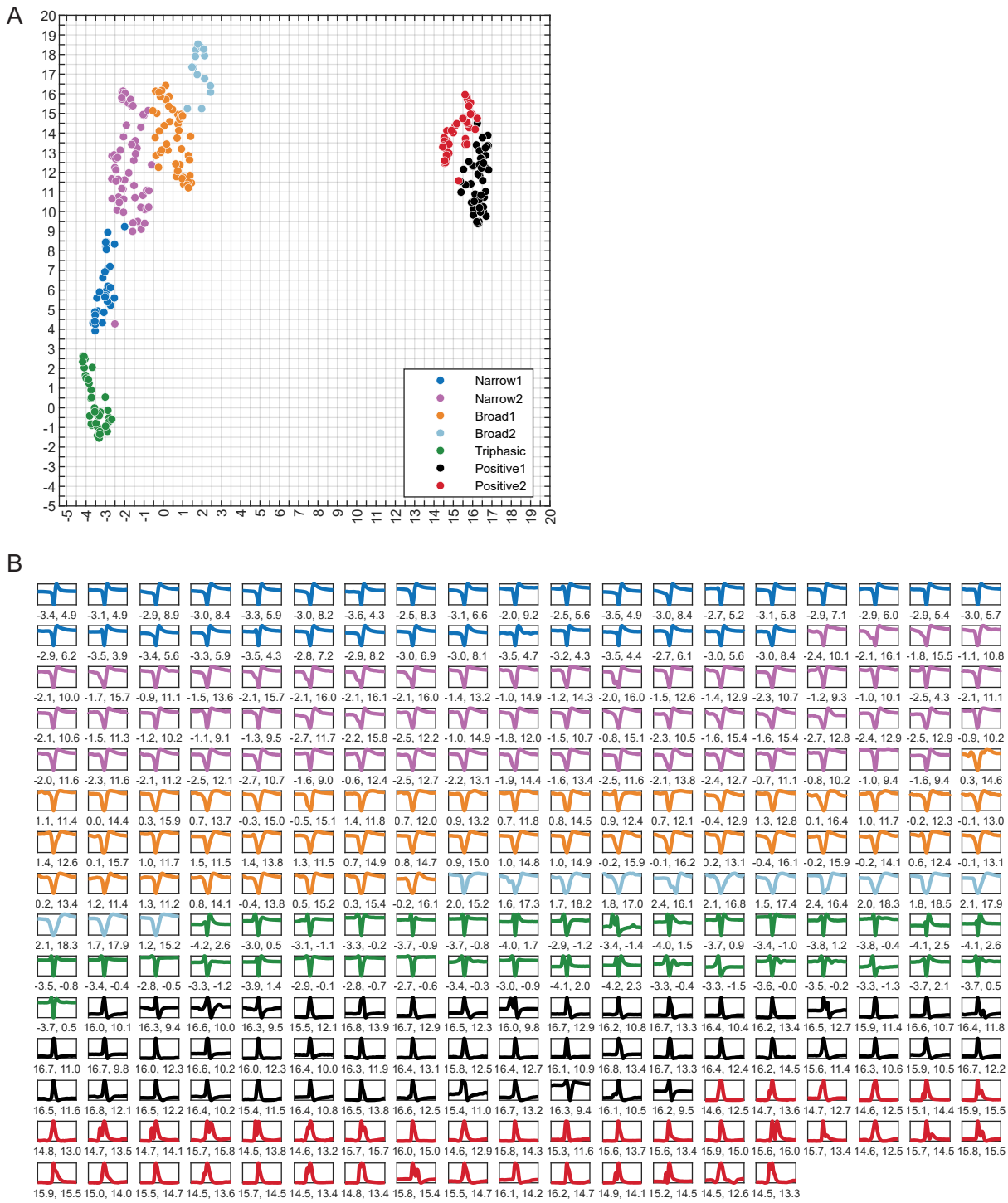

Figure 2-1. All extracellular spike waveforms plotted in **(A)** UMAP space, and **(B)** mean spike waveform traces for each single unit with their corresponding UMAP coordinates. The seven colors refer to the seven waveform classifications from WaveMAP.

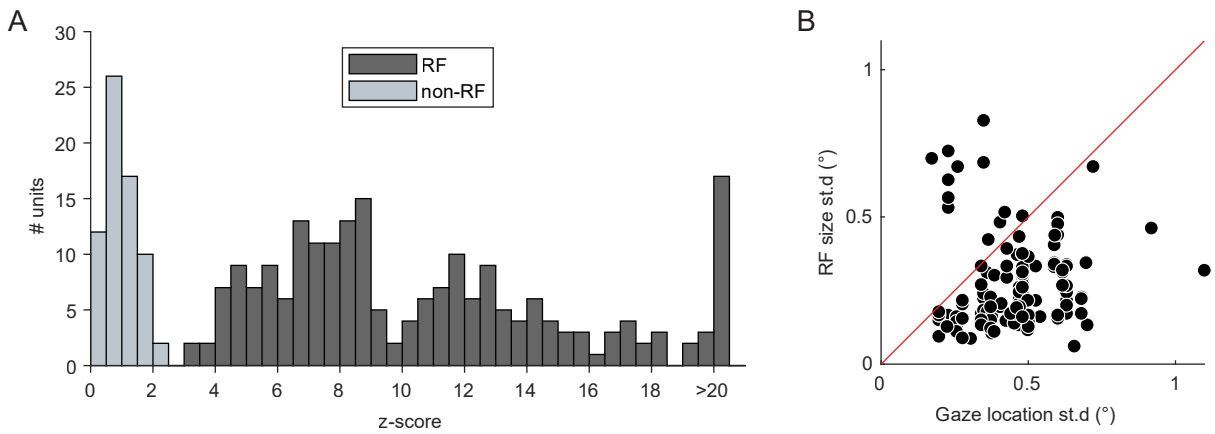

Figure 3-1. Receptive field statistics. **(A)** Distribution of z-scores across all single units. The histogram is binned in size of 0.5 z-score. The black and grey bins refer to RF and non-RF units, respectively. **(B)** Standard deviation of RF size (°) plotted against standard deviation of gaze position (°). The identity line is plotted in red. Nearly all CSTRFs had a lower spatial variance than the gaze location.

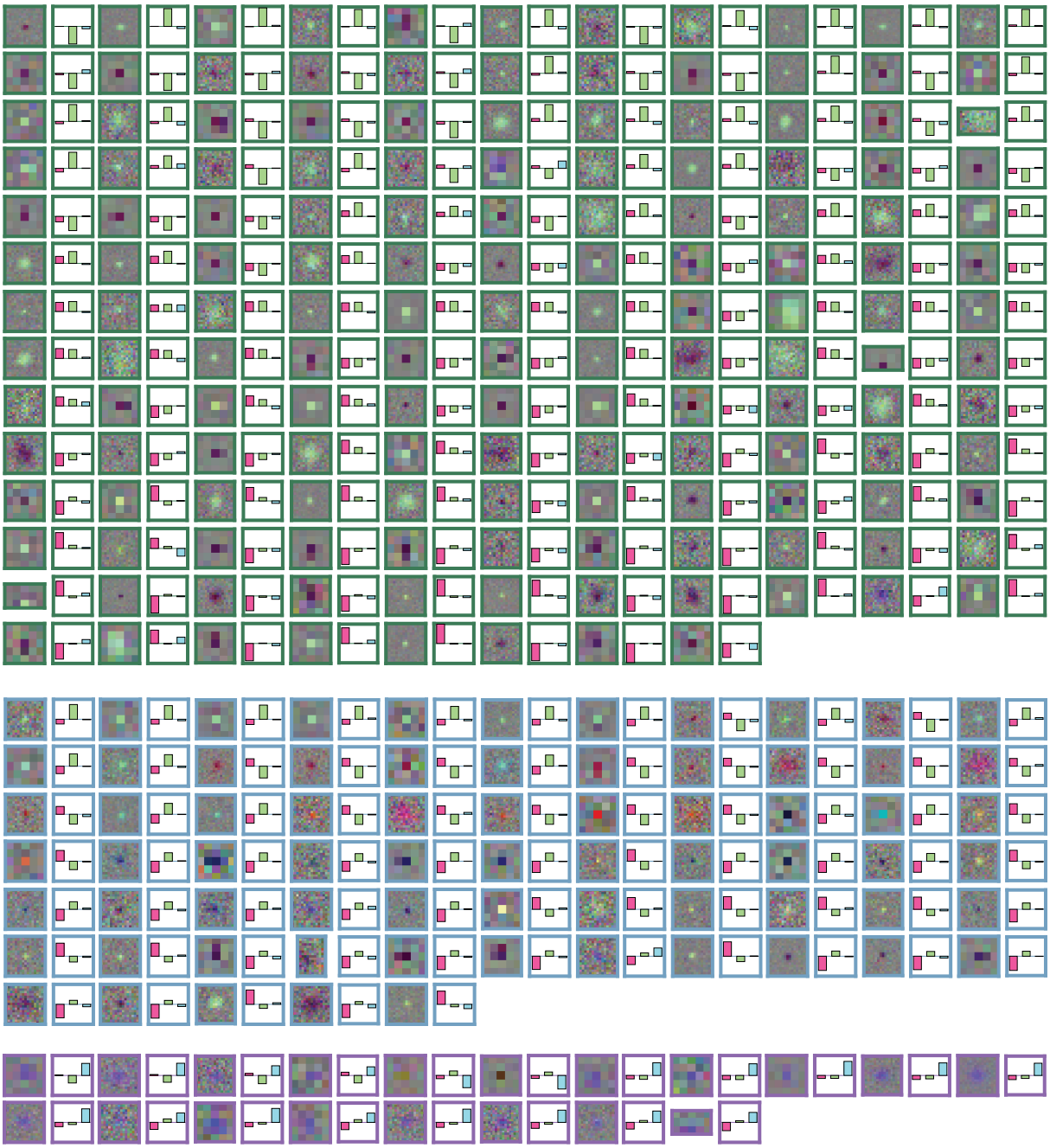

Figure 3-2. RF_{max} and corresponding cone weight from all RF units. RFs are visualized in RGB, and the three cone weights correspond to L, M, and S. The three groups of RFs are M RFs (green border), P RFs (blue border), and K RFs (purple border). All RF plots span 2° in visual space.